

---

## Very high-resolution mapping of emerging biogenic reefs using airborne optical imagery and neural network: the honeycomb worm (*Sabellaria alveolata*) case study

Collin Antoine<sup>1,2,\*</sup>, Dubois Stanislas<sup>3</sup>, Ramambason Camille<sup>1</sup>, Etienne Samuel<sup>1</sup>

<sup>1</sup> Ecole Pratique des Hautes Etudes (EPHE), PSL Research University, Dinard, Brittany, France

<sup>2</sup> Laboratoire d'Excellence CORAIL, Perpignan, France

<sup>3</sup> IFREMER, Laboratoire d'Ecologie Benthique Côtière (LEBCO), Plouzané, France

\* Corresponding author : Antoine Collin, email address : [antoine.collin@ephe.sorbonne.fr](mailto:antoine.collin@ephe.sorbonne.fr)

---

### Abstract :

Biogenic reefs provide a wide spectrum of ecosystem functions and services, such as biodiversity hotspot, coastal protection, and fishing practices. Honeycomb worm (*Sabellaria alveolata*) reefs, in the Bay of Mont-Saint-Michel (France), constitute the largest intertidal bioconstruction in Europe but undergo anthropogenic pressures (aquaculture-stemmed food/space competition and siltation, fishing-driven trampling). Very high-resolution (VHR) airborne optical data enable cost-efficient biophysical measurements of reef colonies, strongly expected for conservation approaches. A synergy of remotely sensed airborne optical imagery, calibration/validation photoquadrat ground-truth (202/101, respectively), and artificial neural network (ANN) modelling is first used to map *S. alveolata* relative abundance, over the largest bioconstruction in Europe. The best prediction of *S. alveolata* abundance was reached with the infrared–red–green (IRRG) spectral combination and ANN model structured with six neurons ( $R^2 = 0.72$ , RMSE = 0.08, and  $r = 0.85$ ). The six hyperbolic tangent formulas were applied to the three input spectral bands (IRRG) in order to build six hidden neuronal images, resulting in VHR digital *S. alveolata* abundance model (6547 × 6566 pixels with 0.5 m pixel size). The innovative model revealed undescribed spatial patterns, namely a reef polarization (perpendicular to the shoreline) of *S. alveolata* abundance: high abundance on forereef and low abundance on backreef.

## 1. Introduction

Coastal reef builders are able to primarily shape the ecology of local environment through the sediment reworking. By trapping and binding carbonate sands, some cyanobacteria and diatoms produce the stromatolites (Andres and Reid 2006), crustose coralline algae form coatings (Gherardi and Bosence 2001), molluscan vermetidae build bioconstructions (Donnarumma et al. 2017), and cnidarian corals create large barriers (Mumby et al. 2003). Less renown despite their very high productivity, annelids (i.e. worms) can create substantial reefs along tropical and temperate coasts (terebellidae: Degraer et al. 2008; serpulidae: Moore et al. 2009; and sabellariidae: Naylor and Viles 2000).

Honeycomb worm reefs erected by the gregarious tube-building polychaete *Sabellaria alveolata* (Linnaeus, 1767) in the megatidal Bay of Mont-Saint-Michel (BMSM, France) consist of the largest intertidal bioconstruction in Europe (Noernberg et al. 2010; Desroy et al. 2011). Contrary to more common encrusting veneers or hummocks on rocky shores, the Sainte-Anne population in the BMSM develops on soft sediment. It is currently structured as three extensive reef entities within the tidal flats. Such biogenic reefs largely contributes to ecosystem functioning and provide a wide panel of ecosystem services: (1) support, with the significant amount of ecological niches (Dubois et al. 2002; Jones et al. 2018); (2) regulation, through the sediment stabilization and trapping (Dubois et al. 2005); and (3) culture, by means of recreational shore fisheries (Plicanti et al. 2016). As a biodiversity hotspot and a rare biological and patrimonial heritage, BMSM worm reefs benefit from the European Habitats Directive

(Council Directive 92/43/EEC) focusing on the protection and “Conservation of Natural Habitats” (“biogenic reefs of open seas and tidal areas”, habitat type 1170). However, Sainte-Anne reefs are threatened by local anthropogenic activities, such as seaward intensive Pacific oyster (*Magallana gigas*) and mussel (*Mytilus edulis*) aquaculture, which increases organic and mineral (silt) seston concentration (Dubois et al. 2009), interspecific competition for food and space by oyster and mussel that colonize reef surface (Dubois et al. 2006), and shell fishing on reefs, that cause fragmentation by trampling and destructive fishing techniques (Plicanti et al. 2016). Pressure synergy has led to a strong reduction in reef health state between 1970 to 2007, as revealed by diachronic estimates of a spatial “Reef Health Status Index” (Desroy et al. 2011).

The previous index is the combination of a set of biological (e.g. epibiont covers) and physical (e.g. fragmentation) features of the reef, aimed at quantifying the health (Desroy et al. 2011). A consortium of European coastal scientists, devoted to honeycomb worm reef conservation, indicate that this index is “a complex time-consuming assessment of the condition of reefs only, that is not widely applicable” ([website: honeycombworms.org](http://www.honeycombworms.org)). Moreover, they advocate that “the usefulness of ... a generic health index for *S. alveolata* reefs ... should not involve laboratory experimentation, complex measurements or time-consuming processing”. Remote sensing techniques hold great promises to address this issue given their non-intrusiveness, ease to use and cost-effectiveness per surface unit (large extent at high resolution). Spaceborne multispectral and hyperspectral, as well as airborne light detection and ranging (LiDAR) and unmanned vehicle (UAV) imageries were successfully utilized for mapping coral reefs (Collin, Hench and Planes 2012; Kutser, Miller and Jupp 2006; Collin et al. 2018a; and Casella et al. 2016), but are still lacking for other reefs, such as annelids. Whereas worm reefs were remotely-sensed by side-scan sound detection and ranging (SoNAR, Moore et al. 2008; Degraer et al. 2008; Raineault, Trembanis and Miller 2012; Pearce et al. 2014) and aerial visible (red-green-blue, RGB) photograph interpretation (Brown and Miller 2011; Godet et al. 2011), only two studies used optical data (including infrared, IR). Satellite multispectral imagery (SPOT-4) enabled *S. alveolata* reefs to be mapped at 20 m pixel size (Marchand and Cazoulat 2003), and airborne combination of RGB photo-interpretation and IR LiDAR elevation data at 2 m pixel size were used to delineate *S. alveolata* reefs’ extent and estimate their volume (Noernberg et al. 2010). However, the application of both studies into a generic health index is challenging insofar as their spatial resolution is too coarse to account for ecophysiology and reef-building activity. More recent high to very high resolution (VHR) spaceborne optical data are not yet available over emerged reefs (lying between 2 and 4 m elevation above the national tidal datum epoch), since they are immersed most of the time. The *Ortholittorale* V2 product, collected by the French Ministry for Ecology, Sustainable Development and Energy (MEDDE) at low tide, remains, to date, the only VHR optical imagery (0.5 m pixel size) available over the honeycomb worm reefs.

Here we created a method for mapping emerging biogenic reefs at VHR using airborne optical image and selected field data, by focusing on *S. alveolata* relative abundance (Saa). The passive, optical imagery (ranging from infrared to blue wavebands at 0.5 m pixel size), acquired from a small aircraft, constitutes the remotely-sensed predictors, and an array of RGB photoquadrats ( $0.5 \times 0.5 \text{ m}^2$ ) is processed to retrieve the Saa relative abundance, as the ground-truth response. Following comparisons of model performance, the ANN is implemented to provide a non-linear

1 regression between both datasets. Our study takes place over Sainte-Anne reefs (Fig. 1a,  
2 1b and 1c), in the heart of BMSM, provided with a maximum tidal range of 14 m.  
3 Despite the interest on a single parameter, the Saa open tubes (Fig. 1d) is deemed as a  
4 good proxy for the reef state, given the threats related to silt sedimentation, oyster and  
5 mussel colonization, as well as man-made physical degradation. This novel approach  
6 has a great potential to contribute to the mapping of worldwide emerging biogenic reefs,  
7 aiming at some health indices. Two methodological issues are raised: what are the best  
8 spectral predictors? What is the optimized model complexity, featured by the number of  
9 neurons? Once the Saa accurately mapped, we examine the spatial patterns of this reef  
10 state proxy. Findings are then discussed from the perspective of stakeholders tasked  
11 with management of the conservation of intertidal biogenic species adversely affected  
12 by anthropogenic activities.

13 Figure 1

## 14 2. Materials and methods

### 15 2.1. Study site

16 Sainte-Anne reefs, composed of three adjacent reefs, are situated on the central part  
17 (48°38'50"N, 1°40'W) of the megatidal (14 m tidal range) Bay of Mont-Saint-Michel  
18 (BMSM). Lying between 2 and 4 m elevation (Noernberg et al. 2010) over the French  
19 hydrographic zero (i.e., national tidal datum epoch), the Sainte-Anne reefs are spreading  
20 over 2.23 km<sup>2</sup> with an estimated volume of 96 301 m<sup>3</sup> (Noernberg et al. 2010). They  
21 face massive mussel farming, structured by rows of wooden piles, lying from 0 to 2 m  
22 elevation. As the largest intertidal bioconstruction in Europe, the Sainte-Anne reef  
23 dynamics can occur in three main morphological shapes (Dubois et al. 2002): isolated  
24 hummocks (ball-shaped structures), coalescent hummocks forming mounds, then  
25 platforms. These three stages are modulated by transitional and degraded intermediate  
26 stages. Each stage is associated with various sessile species assemblages (*M. gigas*, *M.*  
27 *edulis*, *C. fornicata*, green, brown and red macroalgae) and specific demographic  
28 patterns of *S. alveolata*. Sediment grain-size is essentially composed of gravel, sand and  
29 silt classes.

### 30 2.2. Ground-truth *S. alveolata* abundance (Saa) response

31 Fieldwork was carried out on June 26, 2017 using two quadrats (0.5 × 0.5 m<sup>2</sup>, Fig. 2a),  
32 framing RGB photographs, collected with two cameras (Olympus Stylus TG). A series  
33 of 303 photoquadrats, geolocated in the WGS84 datum with GNSS devices (Garmin  
34 eTrex®), were taken, by foot, at spring low tide between UTC 13h and 15h (14h51: 1.3  
35 m water level elevation). Photoquadrats were sampled to encompass the greatest reef  
36 health variability revealed by the most recent mapping work (Rollet et al. 2015). Each  
37 photoquadrat was standardized by the following procedure: (1) correction for the  
38 geometry acquisition through a distortion method carried out with Photoshop® (Fig.  
39 2b), (2) cropping the image within the frame (Fig. 2c), and superimposition of a 5 × 5  
40 grid to analyse independently the 25 image cells (Fig. 2d).

41 The standardized photoquadrat enabled the relative abundance (relative area  
42 covered by various classes in the 0.25 m<sup>2</sup> plot) of two polychaetes (*S. alveolata* and  
43 *Lanice conchilega*), three bivalves (*M. gigas*, *M. edulis* and *C. fornicata*), fleshy

1 macroalgae, dead bivalves, gravel, sand, slit and water classes to be quantified. The  
 2 spatially-dominant class in each of the 25 cells “wins” the cell, and then the relative  
 3 abundance was computed as the sum of the 25 cells divided by 25. We only exploited  
 4 the relative abundance of *S. alveolata* (Saa), by means of open tubes’ recognition. For  
 5 the sake of visual interpretation, eight relative abundances of Saa were visually  
 6 represented by photoquadrats along with their ecological assemblage and reef  
 7 morphology stage, according to Dubois et al. 2002 (Table 1).

8 Figure 2

9 Table 1

### 10 2.3. Optical imagery predictors

11 The airborne optical survey was conducted on September 10, 2014 (UTC 14h00; 0.36 m  
 12 water level elevation) using two full frame charge coupled device (CCD) multispectral  
 13 cameras: one (UltraCam-Xp, 33 mm focal length) acquiring red, green, and blue  
 14 wavebands (RGB, Fig. 3a), and the other one (UltraCam-XpWA, 23 mm focal length),  
 15 collecting infrared, red and green wavebands (IRRG, Fig. 3b). Spectral responses of the  
 16 four optical wavebands are summarized in Table 2. Analog image data are recorded at  
 17 12 bits, converted to digital numbers at 14 bits, stored without compression at 16 bits,  
 18 and finally delivered at 8 bits (USGS 2010). The freely-available *Ortholittorale* V2  
 19 product (see hyperlink in Acknowledgments section) has covered all French coastlines,  
 20 in 2014, with a rigorous acquisition protocol, but does not provide spectral specificities  
 21 of both sensors. The six wavebands, captured with 8-bit radiometric resolution, were  
 22 orthorectified at 0.5 m spatial resolution in the RGF93 datum (GRS80 spheroid)  
 23 projected with Lambert93 (conformal conic), the referential French system. Spectral  
 24 wavebands were highlighted using four spectral signatures associated with four primary  
 25 features (water, sand, reef and algae), easily discriminated though image-based  
 26 inspection (Fig. 3c).

27 Insofar as the objective of this study is to target submeter Saa, a thorough  
 28 registration of coarsely geolocated photoquadrats onto spectral layers was carried out.  
 29 First, the geographic coordinates of ground-truth were converted into the RGF93 datum,  
 30 then projected in Lambert93. Second, the converted geolocations were refined by  
 31 adding the horizontal offset derived from the GNSS measurements and imagery  
 32 geolocations of eight isolated hummocks, clearly distinctive over imagery. Third, the  
 33 submeter registration was achieved by translating, where necessary, the refined  
 34 geolocations onto the correct features using an ultra high resolution UAV-stemmed  
 35 imagery ( $0.08 \times 0.08 \text{ m}^2$ , Collin et al. 2018b).

36 Figure 3

### 37 2.4. Artificial neural network modelling

38 Preliminary comparisons of three main regression learners (ordinary least squares, OLS;  
 39 generalized linear model, GLM; and ANN) were carried out, resulting in the ANN  
 40 selection (Table 3), corroborating another comparison study (Collin, Etienne, and  
 41 Feunteun 2017). The ANN was selected to develop a robust model to link the discrete  
 42 Saa response with continuous multispectral predictors.

43 Based on non-linear modelling,  $h$ , the ANN minimizes least squares using a  
 44 fully-connected single-layer perceptron feed-forward workflow to predict the Saa  
 45 response,  $h(X)$ , from a, activated (hyperbolic tangent function,  $k$ ) sum of the  $i$  (ranging  
 46 from 1 to 7) appropriately weighted,  $w_i$ , neurons,  $n_i$ , resulting themselves from an

appropriate weighting of the multispectral predictors,  $X$  (Heermann and Khazenie 1992):

$$h(X) = k \left( \sum_i w_i n_i(X) \right) \quad (1)$$

Constrained by a single hidden layer, ANN models were developed to test how relevant are the number of neurons, jointly with the implemented spectral combination.

### 2.5. Accuracy assessment

Ground-truth dataset was firstly sorted according to the Saa values, and secondly stratified into 202 calibration and 101 validation subsets (Holdout method) in order to test the acceptability of the modelling. The calibration dataset was subject to 1000 computation runs to reach convergent results and therefore avoid stochastic influences, such as the weight initialization. The matching between observed and predicted Saa, based on the validation dataset, was quantified using the coefficient of determination ( $R^2$ ) and the root mean square error (RMSE) of the corresponding linear regression, as well as the corresponding Pearson product-moment correlation coefficient ( $r$ ).

## 3. Results

### 3.1. Spectral combination and model complexity

The 101 validation values of Saa were negatively correlated with all spectral wavebands ( $r_{\text{Red}} = -0.70$ ,  $r_{\text{Green}} = -0.76$ ,  $r_{\text{Blue}} = -0.74$ ,  $r_{\text{InfraRed}} = -0.58$ ,  $r_{\text{Red}} = -0.68$ ,  $r_{\text{Green}} = -0.74$ ). The influence of the spectral combinations along with the ANN complexity, by interest in the number of neurons in the hidden layer, was tested using the performance metrics of both high  $R^2$  and low RMSE (Fig. 4a). Overall the agreement between observed and predicted Saa was satisfactory, ranging from a  $R^2$  of 0.67 to 0.72 (Fig 4a). The best spectral combination was averagely the IRRG ( $R^2 = 0.71$ ), followed by RGB+IRRG ( $R^2 = 0.70$ ), and finally RGB ( $R^2 = 0.68$ ) (Fig. 4A). The ANN complexity was optimized with six neurons in the intermediate hidden layer ( $R^2 = 0.71$ ) (Fig. 4a). The best ANN model was built using the IRRG spectral combination with the six neurons ( $R^2 = 0.72$ , RMSE = 0.08, and  $r = 0.85$ , Fig. 4b). The architecture of the selected ANN model was represented in order to make explicit the doubling number of neurons, compared to the number of input layers (Fig. 5).

Figure 4

Figure 5

### 3.2. Spatially-explicit modelling of *S. alveolata* abundance (Saa)

The six hyperbolic tangent formulas were applied to the three input spectral bands (IRRG) in order to build six hidden neuronal bands, in turn, implemented into the output linear formula, leading to VHR digital Saa model (Fig. 6,  $6547 \times 6566$  pixels with 0.5 m pixel size).

Figure 6

## 1 4. Discussion

### 2 4.1. Spectral detection of *S. alveolata* abundance (Saa) and socio-ecology

3 The use of the airborne optical imagery (available over all French metropolitan and  
4 most overseas coastal fringes,  $\approx 18\,000$  km, at low spring tide) has enabled the accurate  
5 mapping of the most extended biogenic reef in Europe (i.e., the Sainte-Anne reefs).  
6 Enriching the RGB first product of *Ortholittorale* (2000) by IRRG, the second version  
7 (2014) has leveraged the informational IR waveband. In a broadened context of coastal  
8 biogenic reef mapping, some spectral and spatial lessons can be drawn. The  
9 interpretation of the visible aerial photography, likely to be constrained by the analyst  
10 experience (Brown and Miller 2011, Godet et al. 2011), can be augmented by machine  
11 learning procedures (our ANN and cellular automata modelling from Marchand and  
12 Cazoulat 2003). Contrary to submerged coral reefs, the emerging biogenic reefs can be  
13 better mapped using the IR, strongly absorbed by water and reflected by plant pigment.  
14 Enriching the passive RGB dataset, IR-derived LiDAR topography can measure the  
15 volume of emerging reefs (Noernberg et al. 2010), even if the LiDAR IR intensity has  
16 not been used yet, contrary to salt marshes (Collin, Long and Archambault 2010). The  
17 integration of the active LiDAR IR and G backscatters with the passive RGB imagery is  
18 strongly advocated to refine the emerging reefs, and will be soon possible given the  
19 current airborne topobathymetric LiDAR mapping of French coastal fringe (Litto3D®  
20 website: [diffusion.shom.fr/pro/risques/altimetrie-littorale.html](http://diffusion.shom.fr/pro/risques/altimetrie-littorale.html)). The 0.5 m resolution  
21 encountered in our study outperformed terebellidae and sabellariidae works (100 m in  
22 Godet et al. 2011, 75 m in Rollet et al. 2015 and Desroy et al. 2011, 20 m in Marchand  
23 and Cazoulat 2003, and 2 m in Noernberg et al. 2010).

24 Despite the coarse spectral bandwidths, the signature of the reef indicates a low  
25 reflection in the visible spectrum, with a slight increase from green (G) to infrared (IR)  
26 (Fig. 3c). Increasingly negative correlations between Saa and IR, red (R), blue (B) and  
27 G show that the reef health proxy might be described by a differential variation  
28 occurring between IR and G. Likewise the Normalized Difference Water Index ratioed  
29 the G and IR Landsat TM wavebands (McFeeters 1996). Further spectral investigations,  
30 using a portable hyperspectral sensor, are needed to conclude about the key role played  
31 by water (moisture) in the reef health mapping. The precise spectral signature of Saa  
32 and neighbouring features will also enable a VHR spaceborne proxy to be developed for  
33 worm reefs, as successfully done for coral reefs using WorldView-2 imagery (Collin  
34 and Planes 2012; Collin, Hench, and Planes 2012). The strong negative correlation  
35 between reef health with G might also match the low presence of green macroalgae (e.g.  
36 *Ulva* spp.), as highlighted by a long-term survey of the Sainte-Anne reefs health status  
37 (Desroy et al. 2011). In this respect, BMSM combines high levels of nutrients, as the  
38 junction of landward agricultural runoff and seaward intensive mussel aquaculture, thus  
39 favouring the opportunistic seaweed colonization at the expense of *S. alveolata* open  
40 tubes. Such a calibrated ANN approach should draw attention to focus on the mapping  
41 of green macroalgae. Those fleshy macroalgae have been evidenced to affect  
42 recruitment patterns (Dubois et al. 2006) but also to potentially contribute to the  
43 suspension-feeders' diets, including *S. alveolata* (Lefebvre et al. 2009; Dubois and  
44 Colombo 2014). While eutrophication impacts on *S. alveolata* reefs have not been  
45 investigated, recent studies emphasised adverse effects on coral reefs (Prouty et al.  
46 2017). In a context of ocean acidification, influence on lower pH on this carbonate-rich  
47 reef (made of 60-80% of calcium carbonate grains, Caline et al. 1992) or on biogenic  
48 cement polymerisation (Fournier et al., 2010) consist of relevant research avenues.

Other competitors for space have been targeted, such as farmed *M. gigas* (Desroy et al. 2011), *M. edulis* but also naturally-present *M. galloprovincialis* (Jones et al. 2018), whose spatial distribution could importantly explain reef patterns. Based on the occurrence derived from our ground-truth, we greatly recommend taking the invasive gastropod *C. fornicata* mapping into account, due to its trophic competition as a massive population of suspension-feeders.

#### 4.2. A VHR method to monitor *S. alveolata* abundance (Saa) patterns

Our spatial modelling has enabled the mapping of Saa at VHR using a reliable method. Fieldworks conducted in April 2015 by Rollet et al. (2015), required 15 persons during two days to survey 307 stations using a regular 75 m × 75 m grid mapping (as described in Desroy et al. 2011 for 2001 and 2007 similar survey). Even though such in situ studies have led a comprehensive dataset (sediment, epifauna and health status), the spatial scale at stake conspicuously mismatched the fine-scale patterns of *S. alveolata* ecology.

Our outcomes, based on airborne imagery and two persons during one day for 303 calibration/validation stations, allow reef ecomorphology to be sharply examined, gaining insights into reef responses to exogeneous drivers (Fig. 7). The digital Saa model distinctly elucidates a strong polarization of Saa values: highest Saa at the front of reefs, firstly exposed to sea hydrodynamics and potentially higher coarse sediments and bioclast resuspension (hence increased tube-building activity), contrary to the back of reefs with lowest Saa, lying on more sheltered and muddier environments (Bonnot-Courtois et al. 2008). The back-reef is subject to finer grained resources, which hamper filtration activity as tentacular filaments of *S. alveolata* are clogged and gut contents are more rapidly filled by poor-quality suspended food sources due to an increase in inorganic content (Dubois et al. 2005). Moreover, apparently unhealthy state of the back-reef might be due to the higher occurrences of oysters, hence leading to higher trampling and destructive shell fishing techniques (Plicanti et al. 2016). In addition to the characterization of the reef polarization perpendicular to the shoreline, the VHR Saa mapping feature five separated reefs composing Sainte-Anne (unlike the three main parts identified in Desroy et al. (2011): a central front barrier reef with a vigorous front core and northern small seaward elongations, a northern crescent reef with developed seaward elongations, a southern crescent reef, two massive intermediate (between sea and land) coalescent reefs. Further examinations of landscape connectivity (using dedicated software, such as Graphab) may facilitate modelling of ecological networks and ultimately help stakeholders to include biodiversity conservation into coastal spatial planning.

Figure 7

## 5. Conclusion

This novel research shows that airborne optical imagery, ranging from green to infrared, brings enough information to robustly map emerging biogenic reefs at VHR. The original findings derived from the largest bioconstruction in Europe (honeycomb worm reefs) can be summarized as follows:

- (1) *S. alveolata* relative abundance (Saa) of emerging reefs can be fully surveyed by airborne RGB and/or IRRG cameras at the colony-scale (0.5 m) during low spring tide
- (2) IRRG are better predictors of Saa than RGB ( $R^2 = 0.71$  and  $0.68$ , respectively)



- 1  
2  
3 1 (3) Adding RGB to IRRG reduce the prediction performance of Saa ( $R^2 = 0.70$ )  
4 2 (4) ANN, as a robust non-linear model, is optimized with a hidden layer provided  
5 3 with six neurons in order to predict Saa ( $R^2 = 0.71$ )  
6 4 (5) The best prediction of Saa was reached with the IRRG spectral combination and  
7 5 ANN model structured with six neurons ( $R^2 = 0.72$ , RMSE = 0.08, and  $r = 0.85$ )  
8

## 6 Acknowledgments

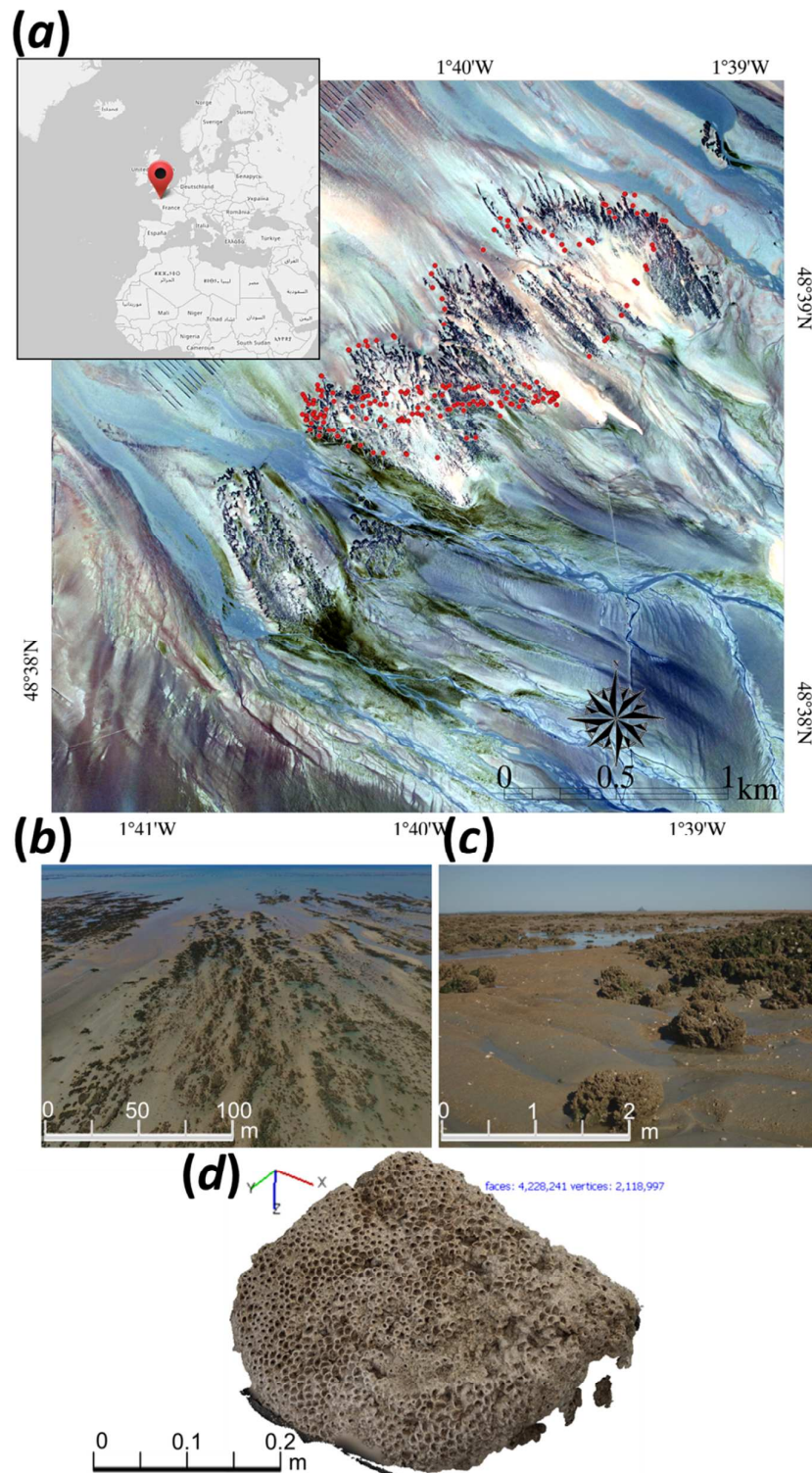
7 Authors gratefully thank French Minister for Ecology, Sustainable Development and Energy for  
8 the airborne multispectral acquisition and dissemination related to *Ortholittorale* V2 product  
9 ([http://cartelie.application.developpement-](http://cartelie.application.developpement-durable.gouv.fr/cartelie/voir.do?carte=telecharg_ol_v2_193&service=CEREMA)  
10 [durable.gouv.fr/cartelie/voir.do?carte=telecharg\\_ol\\_v2\\_193&service=CEREMA](http://cartelie.application.developpement-durable.gouv.fr/cartelie/voir.do?carte=telecharg_ol_v2_193&service=CEREMA)). H el ene Gloria  
11 and Doroth ee James are also greatly acknowledged for their fieldwork involvement.  
12

## 13 References

- 14 Andres, M.S., and R.P. Reid. 2006. "Growth morphologies of modern marine stromatolites: a  
15 case study from Highborne Cay, Bahamas". *Sedimentary Geology* 185(3-4): 319-328.  
16 Bonnot-Courtois C., P. Bassoulet, B. Tessier, F. Cayocca, P. Le Hir, and A. Baltzer. 2008.  
17 "Remaniements s edimentaires superficiels sur l'estr an occidental de la baie du Mont-Saint-  
18 Michel." *European Journal of Environmental and Civil Engineering* 12: 51-65.  
19 Bonnot-Courtois, C., B. Caline, A. L'Homer, and M. Le Vot, M. 2002. "The Bay of Mont-Saint-  
20 Michel and the Rance Estuary, recent development and evolution of depositional  
21 environments". M emoire 26, CNRS, EPHE, TotalFinaElf, Pau, 256 p.  
22 Brown, J.R., and D.C. Miller. 2011. "Persistence and distribution of temperate intertidal worm  
23 reefs in Delaware Bay: a comparison of biological and physical factors". *Estuaries and*  
24 *coasts* 34(3): 583-596.  
25 Caline, B., Y. Gruet, C. Legendre, J. Le Rhun, A. L'Homer, R. Mathieu, and R. Zbinden. 1992.  
26 "The Sabellariid reefs in the Bay of Mont Saint-Michel, France. Ecology, Geomorphology,  
27 Sedimentology and Geologic Implications". Edited and translated by David W. Kirtley,  
28 Florida Oceanographic Society, Contributions to Marine Science 1, Stuart, Florida, 156 p.  
29 Casella, E., A. Collin, D. Harris, S. Ferse, S. Bejarano, V. Parravicini, V., J.L. Hench, and A.  
30 Rovere. 2017. "Mapping coral reefs using consumer-grade drones and structure from motion  
31 photogrammetry techniques". *Coral Reefs* 36(1): 269-275.  
32 Collin, A., and S. Planes. 2012. "Enhancing coral health detection using spectral diversity  
33 indices from worldview-2 imagery and machine learners." *Remote Sensing* 4(10): 3244-  
34 3264.  
35 Collin, A., B. Long, B., and P. Archambault. 2010. "Salt-marsh characterization, zonation  
36 assessment and mapping through a dual-wavelength LiDAR". *Remote Sensing of*  
37 *Environment* 114(3): 520-530.  
38 Collin, A., C. Ramambason, Y. Pastol, E. Casella, A. Rovere, L. Thiault, B. Espiau, G. Siu, F.  
39 Lerouvreur, N. Nakamura, J. Hench, R. Schmitt, S. Holbrook, M. Troyer, and N. Davies.  
40 2018a. "Very High Resolution mapping of coral reef state using airborne bathymetric  
41 LiDAR surface-intensity predictors, visible drone response, and neural network".  
42 *International Journal Remote Sensing* re-submitted.  
43 Collin, A., J.L. Hench, and S. Planes. 2012. "A novel spaceborne proxy for mapping coral  
44 cover." In *Proceedings of the 12<sup>th</sup> International Coral Reef Symposium*, Cairns, 1-5.  
45 Collin, A., S. Dubois, D. James, C. Ramambason, H. Gloria, E. Feunteun, and S. Etienne.  
46 2018b. "Complexit e structurale des r ecifs biog eniques d'hermelles par drone". In *merIG eo*,  
47 *Aix-en-Provence*, 23-26.  
48 Collin, A., S. Etienne, and E. Feunteun. 2017. "VHR coastal bathymetry using WorldView-3:  
49 colour versus learner." *Remote Sensing Letters* 8(11): 1072-1081.  
50 Degraer, S., G. Moerkerke, M. Rabaut, G. Van Hoey, I. Du Four, M. Vincx,... and V. Van  
51 Lancker. 2008. Very-high resolution side-scan sonar mapping of biogenic reefs of the tube-  
52 worm *Lanice conchilega*. *Remote Sensing of Environment* 112(8): 3323-3328.

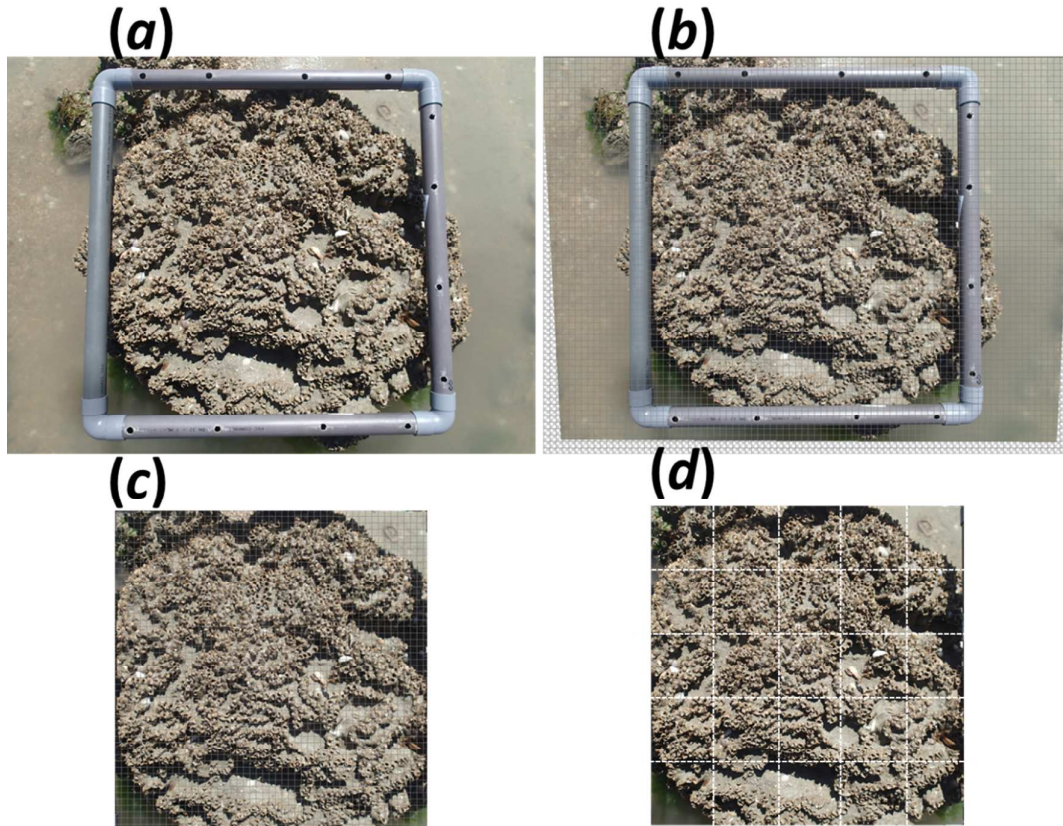
- 1  
2  
3 1 Desroy, N., S. Dubois, J. Fournier, L. Ricquiers, P. Le Mao, P., L. Guérin, L., ... and A.  
4 2 Legendre. 2011. "The conservation status of Sabellaria alveolata (L.)(Polychaeta:  
5 3 Sabellariidae) reefs in the Bay of Mont-Saint-Michel". *Aquatic Conservation: Marine and*  
6 4 *Freshwater Ecosystems* 21(5): 462-471.
- 7 5 Donnarumma, L., R. Sandulli, L. Appolloni, F. Di Stefano, and G.F. Russo. 2017. "Morpho-  
8 6 structural and ecological features of a shallow vermetid bioconstruction in the Tyrrhenian  
9 7 Sea (Mediterranean Sea, Italy)". *Journal of Sea Research*.
- 10 8 Dubois S.F., and F. Colombo. 2014. How picky can you be? Temporal variations in trophic  
11 9 niches of co-occurring suspension-feeding species. *Food Webs* 1: 1-9.
- 12 10 Dubois, S., C. Retière, and F. Olivier. 2002. "Biodiversity associated with Sabellaria alveolata  
13 11 (Polychaeta: Sabellariidae) reefs: effects of human disturbances". *Journal of the Marine*  
14 12 *Biological Association of the United Kingdom* 82(5): 817-826.
- 15 13 Dubois, S., J.A. Commito, F. Olivier, and C. Retière, C. 2006. "Effects of epibionts on  
16 14 Sabellaria alveolata (L.) biogenic reefs and their associated fauna in the Bay of Mont Saint-  
17 15 Michel". *Estuarine, Coastal and Shelf Science* 68(3): 635-646.
- 18 16 Dubois, S., L. Barillé, and B. Cognie, B. 2009. "Feeding response of the polychaete Sabellaria  
19 17 alveolata (Sabellariidae) to changes in seston concentration". *Journal of Experimental*  
20 18 *Marine Biology and Ecology* 376(2): 94-101.
- 21 19 Dubois, S., L. Barillé, B. Cognie, and P.G. Beninger. 2005. "Particle capture and processing  
22 20 mechanisms in Sabellaria alveolata (Polychaeta: Sabellariidae)". *Marine Ecology Progress*  
23 21 *Series* 301: 159-171.
- 24 22 Fournier, J. Etienne, S., and J.B. Le Cam. 2010. "Inter- and intraspecific variability in the  
25 23 chemical composition of the mineral phase of cements from several tube-building  
26 24 polychaetes". *Geobios* 43: 191-200.
- 27 25 Gherardi, D.F.M., and D.W.J. Bosence. 2001. "Composition and community structure of the  
28 26 coralline algal reefs from Atol das Rocas, South Atlantic, Brazil". *Coral reefs* 19(3): 205-  
29 27 219.
- 30 28 Godet, L., J. Fournier, M. Jaffré, and N. Desroy. 2011. "Influence of stability and fragmentation  
31 29 of a worm-reef on benthic macrofauna". *Estuarine, Coastal and Shelf Science* 92(3): 472-  
32 30 479.
- 33 31 Heermann, P. D., and N. Khazenie. 1992. "Classification of multispectral remote sensing data  
34 32 using a back-propagation neural network". *IEEE Transactions on Geoscience and Remote*  
35 33 *Sensing* 30(1): 81-88.
- 36 34 Jones A.G., S.F. Dubois, N. Desroy, and J. Fournier. 2018. "Interplay between abiotic factors  
37 35 and species assemblages mediated by the ecosystem engineer Sabellaria alveolata (Annelida:  
38 36 Polychaeta)". *Estuarine Coastal and Shelf Science* 200: 1-18.
- 39 37 Kutser, T., I. Miller, I., and D.L. Jupp. 2006. "Mapping coral reef benthic substrates using  
40 38 hyperspectral space-borne images and spectral libraries". *Estuarine, Coastal and Shelf*  
41 39 *Science* 70(3): 449-460.
- 42 40 Lefebvre S., J.C. Marin-Leal, S. Dubois, F. Orvain, J.L. Blin, M.P. Bataille, A. Ourry, and R.  
43 41 Galois. 2009. Seasonal dynamics of trophic relationships among co-occurring suspension-  
44 42 feeders in two shellfish-culture dominated ecosystems. *Estuarine Coastal and Shelf Science*  
45 43 82: 415-425.
- 46 44 Marchand, Y., and R. Cazoulat. 2003. "Biological reef survey using spot satellite data  
47 45 classification by cellular automata method – bay of Mont Saint-Michel". *Computers and*  
48 46 *Geosciences* 29:413-421.
- 49 47 McFeeters, S.K. 1996. "The use of normalized difference water index (NDWI) in the  
50 48 delineation of open water features". *International Journal of Remote Sensing* 17: 1425–  
51 49 1432.
- 52 50 Moore, C.G., C. Richard Bates, J.M. Mair, G.R. Saunders, D.B. Harries, and A.R. Lyndon.  
53 51 2009. "Mapping serpulid worm reefs (Polychaeta: Serpulidae) for conservation  
54 52 management". *Aquatic Conservation: Marine and Freshwater Ecosystems* 19(2): 226-236.
- 55 53 Mumby, P.J., W. Skirving, A.E. Strong, J.T. Hardy, E.F. LeDrew, E.J. Hochberg, E. J., ... and  
56 54 L.T. David. 2004. "Remote sensing of coral reefs and their physical environment". *Marine*  
57 55 *pollution bulletin* 48(3-4): 219-228.

- 1  
2  
3 1 Naylor, L.A., and H.A. Viles. 2000. "A temperate reef builder: an evaluation of the growth,  
4 2 morphology and composition of Sabellaria alveolata (L.) colonies on carbonate platforms in  
5 3 South Wales". *Geological Society, London, Special Publications* 178(1): 9-19.
- 6 4 Noernberg, M. A., J. Fournier, S. Dubois, and J. Populus. 2010. "Using airborne laser altimetry  
7 5 to estimate Sabellaria alveolata (Polychaeta: Sabellariidae) reefs volume in tidal flat  
8 6 environments." *Estuarine, coastal and shelf science* 90(2): 93-102.
- 9 7 Pearce, B., J.M. Fariñas-Franco, C. Wilson, J. Pitts, and P.J. Somerfield. 2014. "Repeated  
10 8 mapping of reefs constructed by Sabellaria spinulosa Leuckart 1849 at an offshore wind  
11 9 farm site". *Continental Shelf Research* 83: 3-13.
- 12 10 Plicanti, A., R. Domínguez, S. Dubois, and I. Bertocci. 2016. "Human impacts on biogenic  
13 11 habitats: Effects of experimental trampling on Sabellaria alveolata (Linnaeus, 1767) reefs".  
14 12 *Journal of Experimental Marine Biology and Ecology* 478: 34-44.
- 15 13 Prouty, N.G., A. Cohen, K.K. Yates, C.D. Storlazzi, P.W. Swarzenski, and D. White. 2017.  
16 14 "Vulnerability of Coral Reefs to Bioerosion From Land-Based Sources of Pollution".  
17 15 *Journal of Geophysical Research: Oceans*.
- 18 16 Raineault, N.A., A.C. Trembanis, and D.C. Miller. 2012. "Mapping benthic habitats in  
19 17 Delaware Bay and the coastal Atlantic: acoustic techniques provide greater coverage and  
20 18 high resolution in complex, shallow-water environments". *Estuaries and Coasts* 35(2): 682-  
21 19 699.
- 22 20 Rollet C., D. Mathéron, N. Desroy, and P. Le Mao. 2015. "Suivi de l'état de conservation des  
23 21 récifs d'hermelles (*Sabellaria alveolata*)". Rapport final, décembre 2015,  
24 22 Ifremer/ODE/LITTORAL/LER/BN-15-008, Projet Life 12 ENV/FR/316 – Expérimentation  
25 23 pour une gestion durable et concertée de la pêche à pied de loisir – LIFE+ Pêche à pied de  
26 24 loisir, 32 p. + annexes.
- 27 25 United States Geological Survey. 2010. "Digital aerial sensor certification report for the  
28 26 Microsoft Vexcel UltraCamD, UltraCamX, UltraCamXp, and UltraCamXp WA Models".  
29 27 Department of the Interior US Geological Survey, 19 p.
- 30  
31  
32  
33  
34  
35  
36  
37  
38  
39  
40  
41  
42  
43  
44  
45  
46  
47  
48  
49  
50  
51  
52  
53  
54  
55  
56  
57  
58  
59  
60

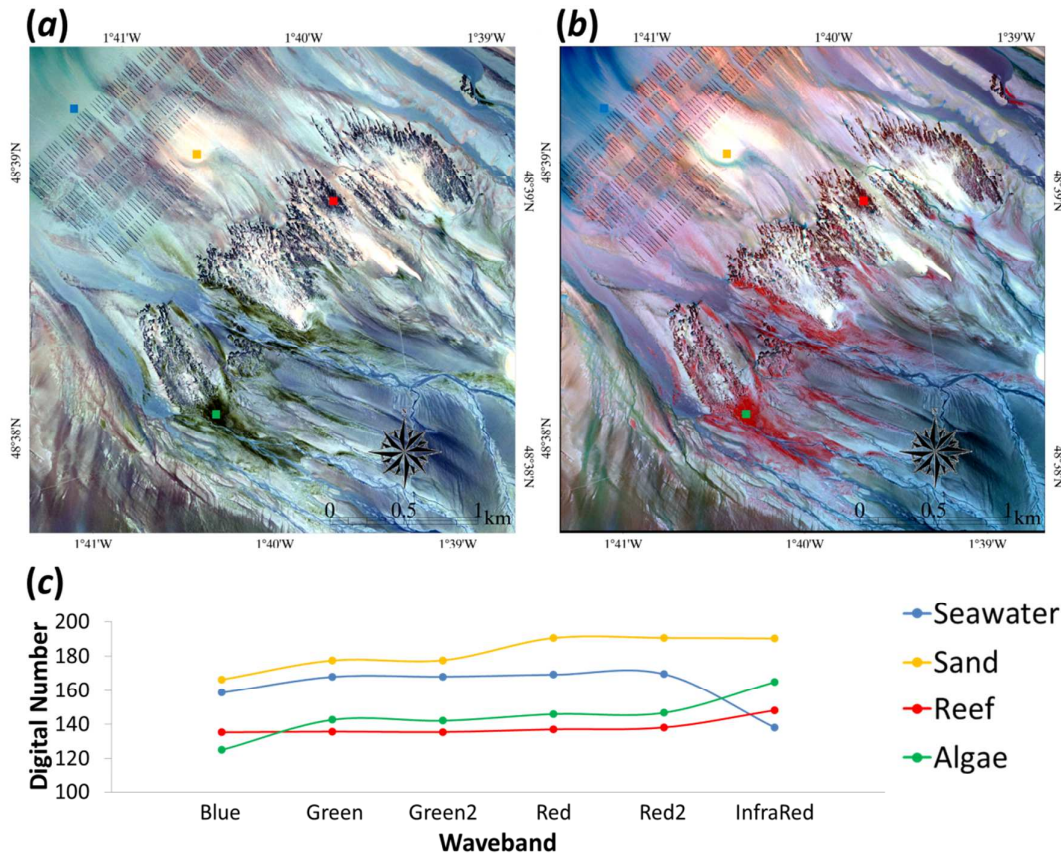


**Figure 1.** (a) Natural-coloured (red-blue-green) airborne imagery ( $6547 \times 6566$  pixels with 0.5 m pixel size) collected on September 10, 2014, over the location of Sainte-Anne three honeycomb worm reefs (*Sabellaria alveolata*), within Bay of Mont-Saint-Michel (Brittany-Normandy, France). Red spots represent photoquadrat locations. (b) Natural-coloured airborne UAV oblique imagery over a portion of the Sainte-Anne reefs. (c) Natural-coloured handborne imagery inside the Sainte-Anne reefs. (d) 3D-model of a honeycomb worm hummock colony draped with natural-coloured imagery.

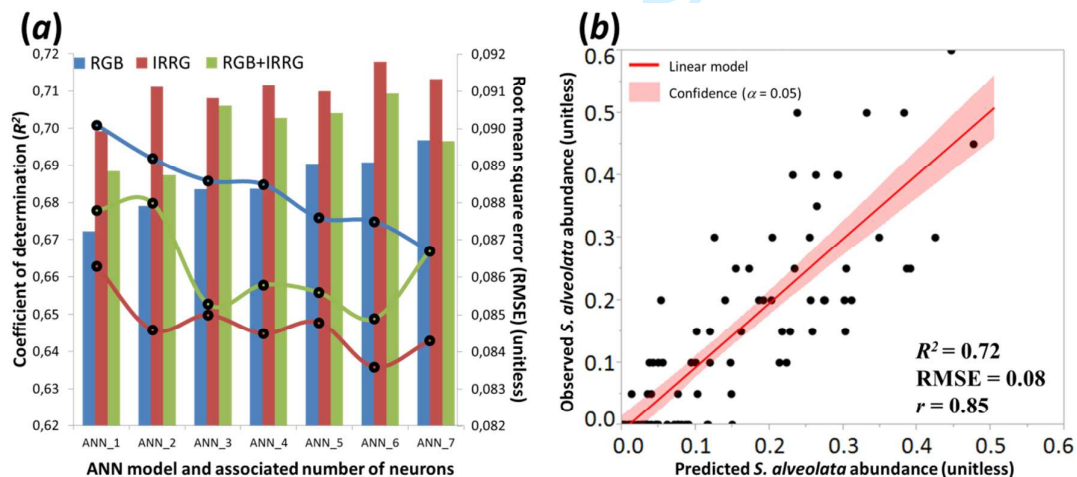
1



2  
3 **Figure 2.** Standardization procedure applied to the (a) original photoquadrat, (b) to correct for  
4 the distortion, (c) to crop at the frame scale ( $0.5 \times 0.5 \text{ m}^2$ ), and (d) to apply a  $5 \times 5$  grid.  
5  
6  
7  
8  
9

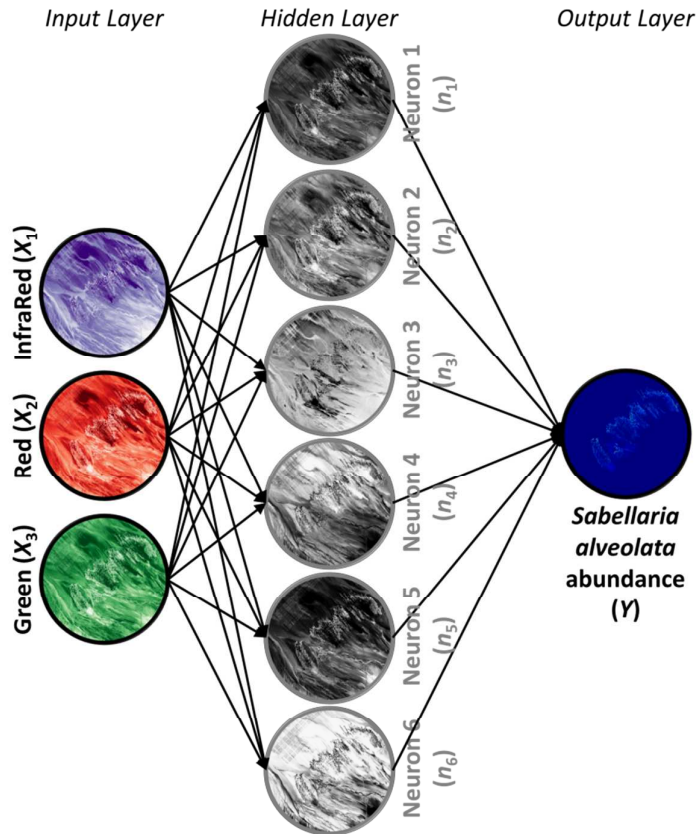


**Figure 3.** (a) Natural-coloured (red-blue-green), and (b) infrared-coloured (infrared-red-green) airborne imageries ( $6547 \times 6566$  pixels with 0.5 m pixel size) collected on September 10, 2014, over the location of Sainte-Anne reefs. (c) Four rectangles were selected by visual inspection for determining spectral signatures based on *Ortholittorale* V2 of seawater (blue), sand (yellow), reef (red), and algae (green).



**Figure 4.** (a) Bar and line plot of the performance (coefficient of determination,  $R^2$ , and root mean square error, RMSE, respectively) of the 21 artificial neural network (ANN) models predicting the validation dataset of *Sabellaria alveolata* abundance ( $N = 101$ ), as functions of spectral combination inputs and number of hidden neurons. (b) Scatterplot of the validation versus predicted *S. alveolata* abundance based on the best ANN model (IRRG as input layers and six neurons within hidden layer).

1



2

3

**Figure 5.** Conceptual flowchart of the artificial neural network modelling based on the infrared, red and green input layers, the hidden layer provided with six neurons to be able to predict the *Sabellaria alveolata* abundance.

4

5

6

7

8

9

10

11

12

13

14

15

16

17

18

19

20

21

22

23

24

25

26

27

28

29

30

31

32

33

34

35

36

37

38

39

40

41

42

43

44

45

46

47

48

49

50

51

52

53

54

55

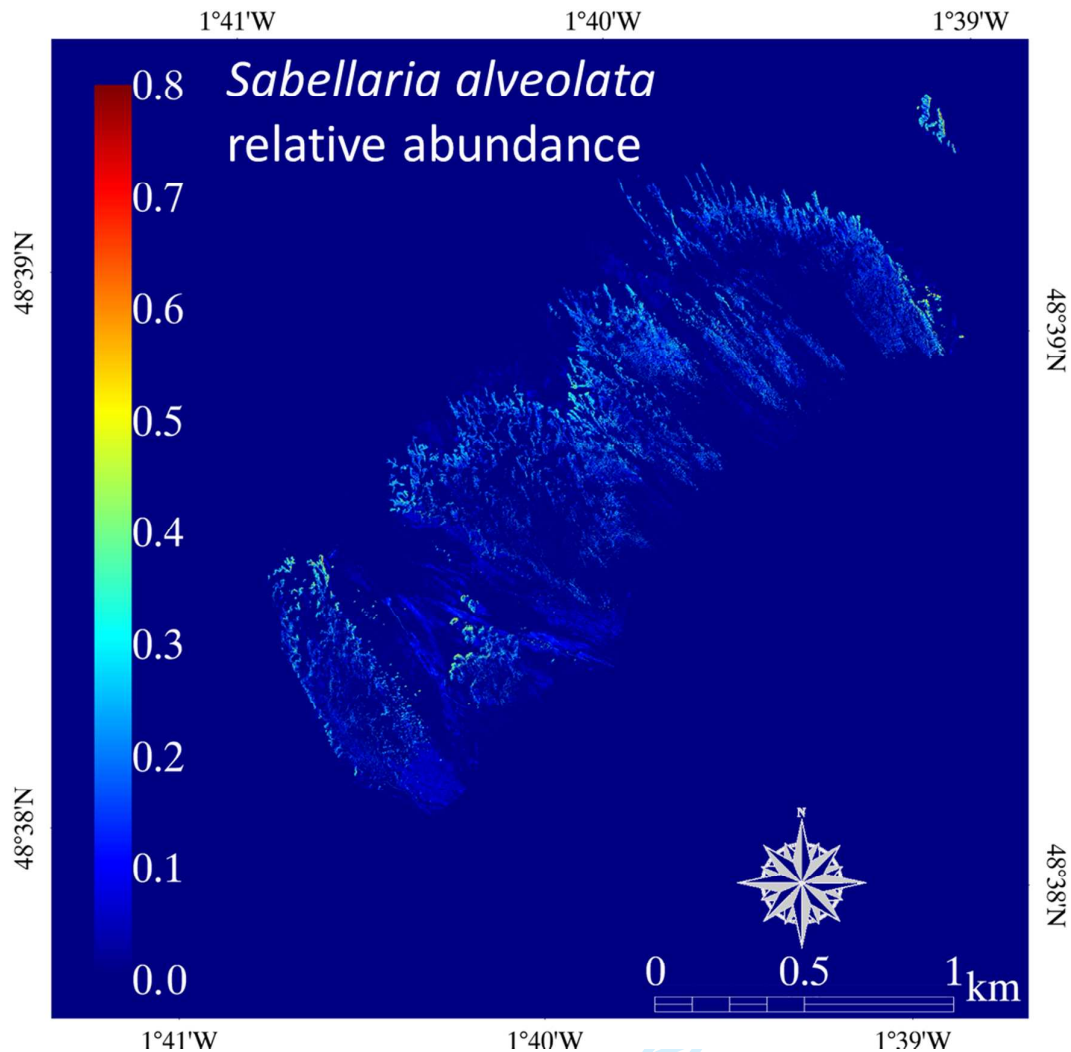
56

57

58

59

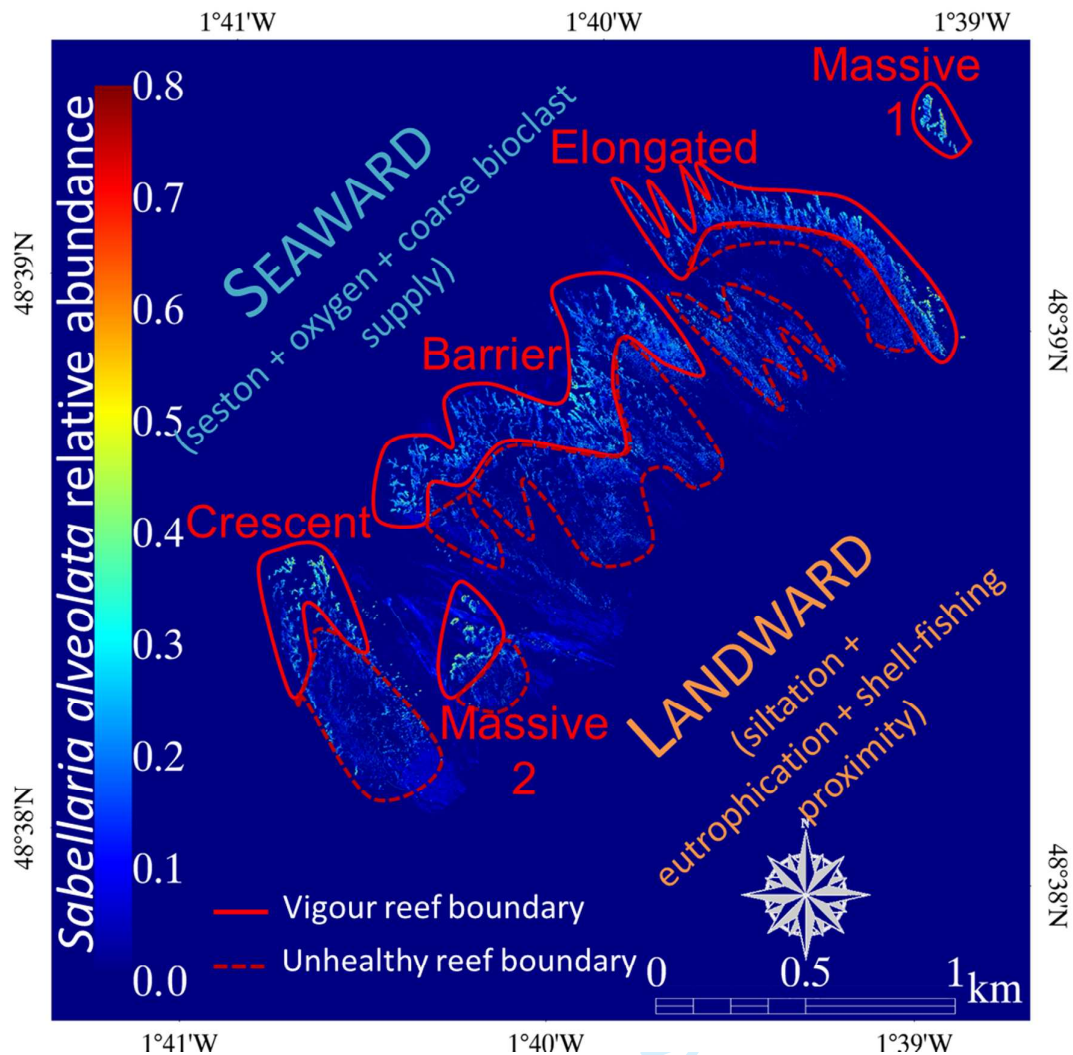
60



**Figure 6.** Digital *Sabellaria alveolata* abundance model derived from artificial neural network model with airborne infrared, red and green bands as input layers and six neurons within hidden layer (6547 × 6566 pixels at 0.5 m pixel size).

1  
2  
3  
4  
5  
6  
7  
8  
9  
10  
11  
12  
13  
14  
15  
16  
17  
18  
19  
20  
21  
22  
23  
24  
25  
26  
27  
28  
29  
30  
31  
32  
33  
34  
35  
36  
37  
38  
39  
40  
41  
42  
43  
44  
45  
46  
47  
48  
49  
50  
51  
52  
53  
54  
55  
56  
57  
58  
59  
60


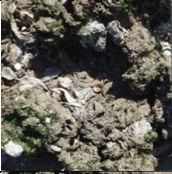










**Figure 7.** Synthetic conceptual diagram proposing explanation factors of polarized *Sabellaria alveolata* abundance in Sainte-Anne reefs, based on the model derived from artificial neural network model with airborne infrared, red and green bands as input layers and six neurons within hidden layer (6547 × 6566 pixels at 0.5 m pixel size).

1  
2  
3  
4  
5  
6  
7  
8  
9  
10  
11  
12  
13  
14  
15  
16  
17  
18  
19  
20  
21  
22

**Table 1.** Ecological description of the georeferenced photoquadrats ( $N = 303$ ,  $0.5 \times 0.5 \text{ m}^2$ ) from which the abundance of *Sabellaria alveolata* open tubes was retrieved, as a proxy for the honeycomb worm reef state.

Photoquadrat-based class	Ecological assemblage	<i>Sabellaria alveolata</i> relative abundance	Worm reef morphology stage (Dubois et al. 2002)	Colour ramp
	Sand/silt with dead bivalves (shells)	0.0	No <i>S. alveolata</i> presence	
	<i>M. gigas</i> / <i>M. edulis</i> / <i>C. fornicata</i> / fleshy macroalgae / sand / silt / <i>S. alveolata</i>	0.1	Degraded isolated <i>S. alveolata</i> hummock	
	<i>S. alveolata</i> / sand / silt / <i>M. gigas</i> / <i>M. edulis</i> / <i>C. fornicata</i> / fleshy macroalgae	0.2	Isolated <i>S. alveolata</i> hummock	
	<i>S. alveolata</i> / sand / silt / shells	0.3	Isolated <i>S. alveolata</i> hummock	
	<i>S. alveolata</i> / sand / silt / shells	0.4	Isolated <i>S. alveolata</i> hummock	
	<i>S. alveolata</i> / silt / shells	0.5	Coalescent <i>S. alveolata</i> hummock	
	<i>S. alveolata</i> / silt / shells	0.6	<i>S. alveolata</i> mound	
	<i>S. alveolata</i>	0.7	<i>S. alveolata</i> platform	

**Table 2.** Spectral sensitivity (in nm) of the airborne optical cameras (UltraCam-Xp and UltraCam-XpWA provided with focal lengths of 33 and 23 mm, respectively).

Blue	Green	Red	InfraRed
410-540	480-630	580-700	690-1000

**Table 3.** Preliminary results of the performance (coefficient of determination,  $R^2$ ) of three regression models predicting the validation dataset of *Sabellaria alveolata* abundance ( $N = 101$ ), in respect to the spectral combination inputs.

Spectral datasets	Ordinary Least Squares	Generalized Linear Model (Poisson)	Artificial Neural Network (3 neurons)
RGB	0.66	0.57	0.69
IRRG	0.65	0.36	0.70
RGB+IRRG	0.63	0.37	0.70